ACS Partner Journal
PRECISION CHEMISTRY

Open Access
This article is licensed under CC-BY-NC-ND 4.0

pubs.acs.org/PrecisionChem
Article

Management of Platinum Electronic States through Metal Host–Guest Interactions for Enhanced Oxygen Reduction

Yudan Chen,[▽] Yuanhua Sun,[▽] Sicheng Li,[▽] Xiaokang Liu, Wei Zhang, Qiquan Luo, Dong Liu,* Tao Ding,* and Tao Yao*

Cite This: *Precis. Chem.* 2025, 3, 279–288

Read Online

ACCESS | Metrics & More | Article Recommendations | Supporting Information

ABSTRACT: Controlling the electronic states of Pt-based catalysts holds great promise for enhancing the intrinsic activity of the oxygen reduction reaction (ORR). Herein, inspired by first-principles simulations, we propose a strategy using metal host–guest interactions to tune Pt 5d electronic characteristics to optimize the adsorption strength of the key *OH intermediate. The hybrid electrocatalyst of Pt nanoparticles on a single-atom Co–N–C support (Pt@Co_L SAs) exhibits a half-wave potential of 0.92 V and a mass activity of 3.2 A·mg_{Pt}^{-1} at 0.9 V in 0.1 M $HClO_4$, which is a 20-fold enhancement compared with commercial Pt/C. Impressively, the Pt loading in the catalyst is as low as 1.70 wt %, which represents the lowest value reported in the relevant literature on Pt-based acidic ORR catalysts. Comprehensive spectroscopy investigations and theoretical simulations revealed that the precise regulatory effect of Co in various dispersion states effectively weakens the intermediate adsorption and reduces the energy barrier for the water decomposition step. Our finding provides valuable insights for the development of advanced ultralow-Pt ORR catalysts via the integration engineering of multiple metal sites.

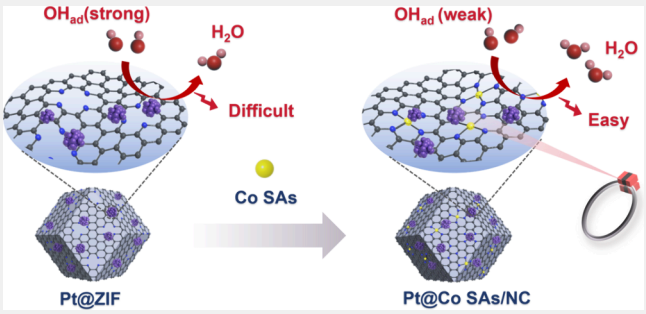

KEYWORDS: *ultralow-platinum catalyst, regulating electronic states, host–guest interaction, intermediate adsorption weakening, oxygen reduction reaction*

INTRODUCTION

Developing low-cost and high-performance cathodic oxygen reduction reaction (ORR) catalysts is crucial for advancing proton exchange membrane fuel cells (PEMFCs).[1,2] Platinum group metals (PGM) are the most efficient catalysts for fuel cells.[3] However, PGM catalysts not only are expensive but also suffer from instability under harsh conditions, posing challenges for large-scale commercial applications.[4,5] Fortunately, Pt-based nanoparticle catalysts derived from metal–organic frameworks (Pt@ZIF) have demonstrated a large specific surface area and uniform distribution of active sites on electrodes. These distinctive characteristics enable them to exhibit superior activity in fuel cells in comparison to conventional carbon carriers.[6] Nevertheless, Pt@ZIF typically exhibits excessive adsorption of intermediates such as *OH, which can block the active site and hinder the generation of *OH and *OOH and their conversion to H_2O, thereby decreasing the reactivity (Figure 1a).[7,8] In order to overcome these issues, it is crucial to reduce the Pt loading while electronically modulating the active site of Pt to mitigate *OH adsorption and expose more Pt active sites, thus, promoting the Pt utilization and the intrinsic activity. Indeed, it has been reported that addressing these issues can be achieved by alloying Pt with transition metals[9−11] and developing PGM-free catalysts.[12,13] However, these catalysts still face challenges of activity degradation and stability decline in the ORR process.

Transition metal and nitrogen codoped carbon (M–N–C) demonstrates remarkable activity and stability owing to the strong metal–support interactions.[14] Its incomplete d-orbitals can readily accept electrons provided by *O intermediates, effectively lowering the potential barrier of the activation energy.[15] If the ultralow Pt-loaded catalyst and M–N–C can compensate for each other through synergistic effects, it will not only significantly reduce the amount of Pt used but also weaken the intermediate adsorption strength and maintain excellent activity and durability.[16] Notably, the higher equilibrium potential of Co^{3+}/Co^{2+} in Co–N–C prevents susceptibility to Fenton's reaction, enabling superior isolation and anchoring of the Pt nanoparticles (NPs) compared to the other M–N–C, thereby finely tuning the electronic structure

Received: September 21, 2024
Revised: February 15, 2025
Accepted: February 17, 2025
Published: March 3, 2025

ACS Publications
© 2025 The Authors. Co-published by University of Science and Technology of China and American Chemical Society

https://doi.org/10.1021/prechem.4c00073
Precis. Chem. 2025, 3, 279–288

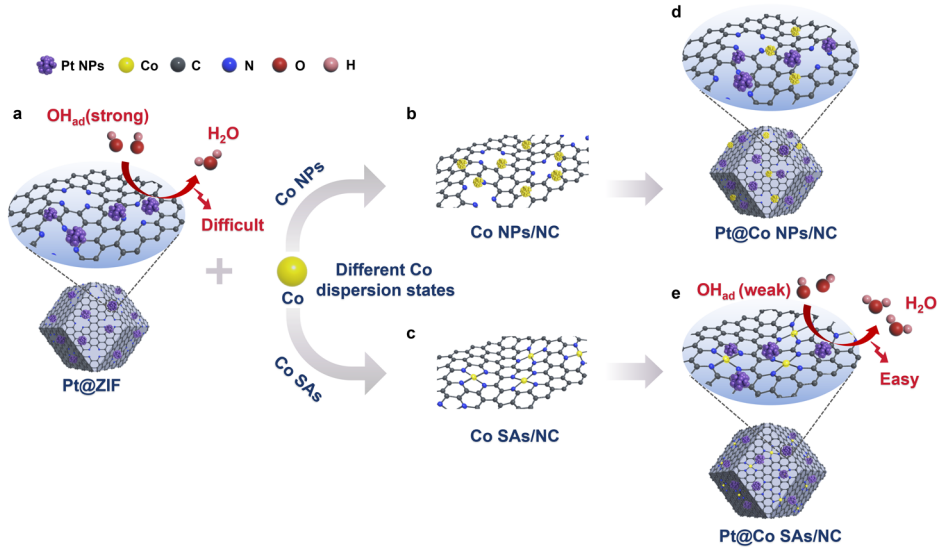

Figure 1. Schematic representation of the different Co dispersion states affecting *OH intermediate adsorption on Pt NPs. (a) Schematic representation of the ultimate water decomposition of Pt@ZIF. (b) Schematic representation of Co NPs/NC. (c) Schematic representation of Co SAs/NC. (d) Schematic representation of Pt@Co NPs/NC. (e) Schematic representation of the ultimate water decomposition of Pt@Co SAs/NC.

of Pt NPs.[17−19] Meanwhile, the host−guest interaction between Co−N−C and Pt NPs will enhance the electron transfer efficiency, reduce the intermediate adsorption energy, and greatly improve the catalytic activity and durability. While the doping effect of Co−N−C in Pt has been confirmed by relevant research reports,[20] there is still a lack of detailed and clear research on how different dispersion states of Co specifically modulate the electronic structure of Pt NPs and their intermediate adsorption (Figures 1b and 1c). Therefore, effectively designing catalysts of Pt nanoparticle catalysts with nearby dispersed Co states to regulate intermediate adsorption and verify the synergistic effects reliably remains a significant challenge (Figures 1d and e).

In this work, guided by preliminary theoretical calculations, we meticulously designed a Pt-based catalyst, integrating different dispersion states of Co alongside the Pt nanoparticles. To facilitate the differentiation, the samples doped with higher and lower amounts of cobalt single atoms were named Pt@Co_H SAs and Pt@Co_L SAs. The samples doped with cobalt nanoparticles were named as Pt@Co NPs. Comprehensive density functional theory (DFT) calculations confirmed that at low Pt loadings, and doping with trace Co single atom can effectively weaken the adsorption capacity of the *OH intermediate, resulting in excellent mass activity, stability, and robust resistance to methanol poisoning in acidic electrolytes. Furthermore, related characterizations, such as *ex situ* X-ray absorption fine structure (XAFS) and X-ray photoelectron spectroscopy (XPS), revealed that the Pt@Co_L SAs sample exhibited superior performance due to the lower valence state of Pt. Specifically, an increase in the Co−N coordination number led to a corresponding decrease in the Pt−N coordination number, thereby reducing the valence state of Pt. Interestingly, during performance testing, it was observed that reduced Co doping leads to a lower Pt valence state. These noteworthy findings were further corroborated by *in situ* characterization experiments, including *in situ* XAFS and synchrotron radiation infrared (SR-IR), which illustrated that the regulating Co single atoms (Co SAs) can effectively weaken the *OH adsorption on Pt, thereby reducing the energy barrier for the ultimate water decomposition step in the ORR process. Our findings might contribute to a deeper understanding of how transition metals in different dispersion states modulate noble metal nanoparticles, potentially advancing the catalyst design for various applications.

RESULTS AND DISCUSSION

Preliminary Theoretical Calculation

First, theoretical calculations were conducted to evaluate the potential impact of differently dispersed Co doping on regulating the adsorption of intermediates on Pt NPs, aiming to gain a deeper understanding of how the host−guest interaction between Pt and single-atom Co enhances catalytic activity effectively. A simplified composite model of Pt@Co_L SAs was constructed by coupling a Pt cluster model with a monolayer graphene model featuring isolated Co−N_4 sites. Additionally, considering the disparate effects of different dispersion states on intermediate adsorption, calculations were conducted on both Pt@Co_H SAs and Pt@ZIF to elucidate their differences and explore the three key intermediates of the ORR process.[21] The 4e$^-$ ORR process is illustrated in Figure 2a, in which active metal atoms were identified as potential adsorption sites for reactants and key oxygenated intermediates. Specifically, according to the ORR free energy diagram in Figure 2b, the generation of H_2O molecules from *OH represents the rate-determining step (RDS). It is pertinent to mention that Pt@Co_L SAs exhibits the lowest RDS free energy, measuring only 0.68 eV at U = 1.23 V, indicating that Co SAs are the optimal choice for regulating the adsorption energy of the intermediates and accelerating the ORR 4e$^-$ process on the Pt sites. Furthermore, differential charge densities in Figure 2c and Figure S1 reveal that Pt@Co_L SAs exhibits significantly less charge transfer to *OH compared to Pt@Co_H SAs and Pt@ZIF. The strong host−guest interaction between Pt and Co−N_4 sites results in the formation of electron-enriched Pt sites with weakened adsorption to key *OH intermediates and reduces the reaction energy barrier. This corresponds to the weakest adsorption of the *OH intermediate by Pt@Co_L SAs in the free energy diagram. To gain further insights into the enhanced ORR activity of Pt@Co_L SAs, we examined the

https://doi.org/10.1021/prechem.4c00073
Precis. Chem. 2025, 3, 279−288

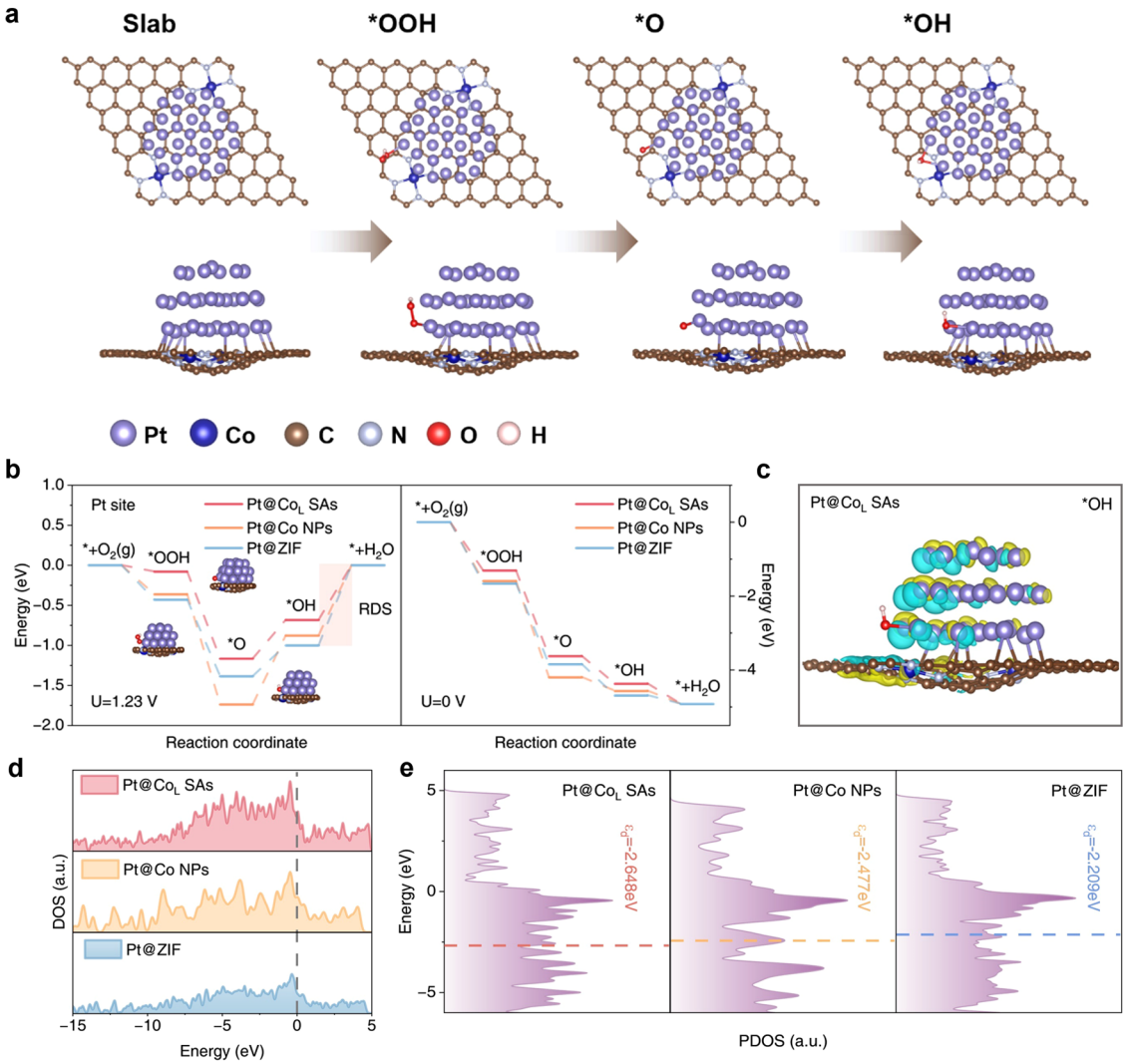

Figure 2. DFT calculations of the ORR activity. (a) The ORR 4e$^-$ reaction process. (b) ORR free-energy diagrams at 1.23 V (left) and 0 V (right) for Pt@Co$_L$ SAs, Pt@Co NPs, and Pt@ZIF. (c) Differential charge densities of Pt@Co$_L$ SAs. The blue and yellow surfaces represent electron depletion and electron accumulation, respectively. (d) TDOS and (e) PDOS of Pt@Co$_L$ SAs, Pt@Co NPs, and Pt@ZIF. Pt (purple), Co (dark blue), N (pale gray), C (brown), O (red), and H (pale pink).

electronic interactions between Pt and Co through the total density of states (TDOS) and the corresponding d-band center of active atoms.

As shown in Figure 2d, Pt@Co$_L$ SAs sample exhibits the largest density of states at the Fermi energy level, revealing the strongest charge transfer capability.[22] Correspondingly, the projected density of states (PDOS) reveals that the d-band center of Pt@Co$_L$ SAs is located farther from the Fermi energy level (−2.648 eV) compared to Pt@Co$_H$ SAs and Pt@ZIF, demonstrating the weakened adsorption of *OH on Pt (Figure 2e and Figure S2).[23] In summary, Co SAs are the most effective at modulating the *OH adsorption energy, reducing the charge accumulation on Pt. Synergistic electronic interactions between Co SAs and Pt catalytic sites are expected to weaken the adsorption of the key intermediate OH* and reduce the final reaction energy barrier. Inspired by the results of DFT calculations, the high-performance oxygen reduction catalysts modulated by Co in different dispersion states were prepared via a two-step annealing method. First, the precursor ZnCo-ZIF was synthesized via a zeolitic imidazoline framework (ZIF-8), then abundant single-atom Co sites were embedded through a pyrolysis process to obtain Co-SAs-NC. The as-obtained powder was dispersed in the H_2PtCl_6 solution, where the Co single-atom sites further reacted with $PtCl_6^{2-}$ ions.[24] Finally, thermal reduction in a reducing atmosphere was applied to achieve the Pt NPs anchored by Co single atoms (Pt@Co$_L$ SAs). A series of different Pt-based catalysts were synthesized by varying Co content, named Pt@Co$_L$ SAs, Pt@Co$_H$ SAs, and Pt@Co NPs, for comparison. Additionally, Pt@ZIF without Co was also synthesized.

Structural and Morphological Characteristics

Inductively coupled plasma−atomic emission spectrometry (ICP-AES) was used to determine the contents of Pt and Co elements in the catalysts (Table S1), revealing that the Pt@Co$_L$ SAs sample contains 1.7 wt % Pt. As shown in the X-ray diffraction (XRD) patterns (Figure S3), Pt@Co$_L$ SAs sample exhibits a broad peak around 25°, which is attributed to the (002) plane of the carbon. The diffraction peaks located at 39.9°, 46.4°, and 67.8° belong to the (111), (200), and (220) planes of face-centered cubic Pt, respectively.[25,26] The XRD pattern of Co SAs-ZIF-NC showed no sharp peaks, indicating the absence of a long-range ordered crystal structure. Instead,

https://doi.org/10.1021/prechem.4c00073
Precis. Chem. 2025, 3, 279−288

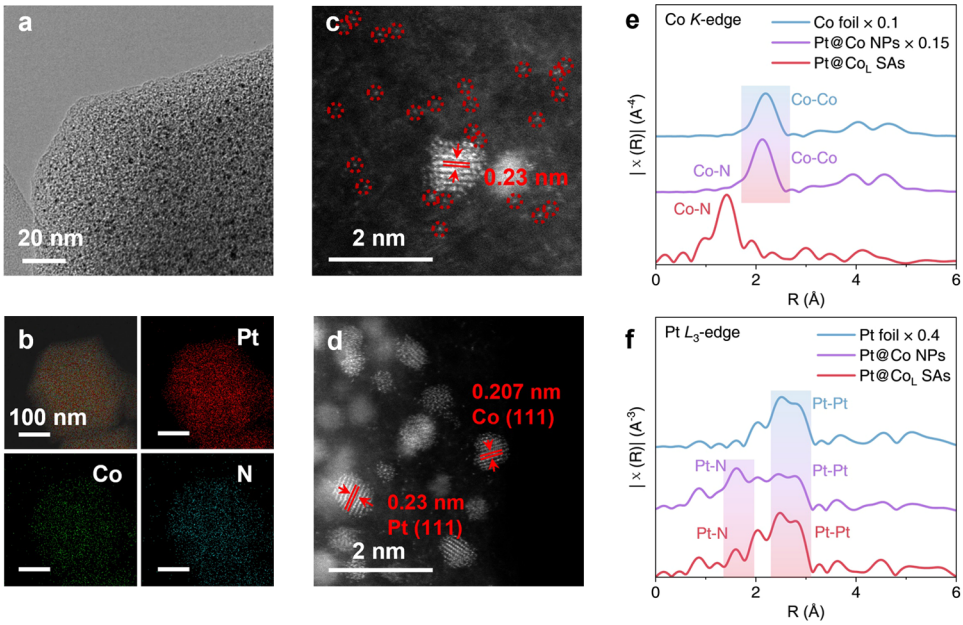

Figure 3. Structural and morphological characteristics. (a) TEM image of Pt@Co_L SAs. (b) EDX mappings of Pt@Co_L SAs showing the uniform dispersion of Pt (red), Co (green), and N (cyan), respectively. HAADF-STEM images of (c) Pt@Co_L SAs and (d) Pt@Co NPs. EXAFS spectra of the (e) Co K edge and (f) Pt L_3 edge for Pt@Co_L SAs, Pt@Co NPs, and reference samples.

only two broad diffraction peaks at about 25° and 43° are observed, corresponding to the (002) and (101) planes of amorphous carbon, respectively.[27] As shown in Figure 3a, the transmission electron microscopy (TEM) image revealed that Pt NPs were uniformly dispersed on the surface of Co SAs-ZIF-NC. High-resolution TEM (HRTEM) images in Figure S4 indicated that the size of Pt NPs in Pt@Co_L SAs was mainly concentrated at 1−2 nm. Energy-dispersive X-ray (EDX) spectroscopy mappings (Figure 3b) further demonstrated the homogeneous distribution of Pt and Co. A comparable distribution of Pt particles was observed in the Pt@Co_H SAs (Figures S5 and S6). In contrast, as the Co content in Pt@Co NPs increased, the dispersion state of Co changed, resulting in the aggregation of Co NPs (Figures S7 and S8). Raman spectroscopy provided insight into the fundamental characteristics of the carbon matrix. Within the detection range, two distinct spectral bands corresponding to the D-band (1350 cm^{-1}) and G-band (1586 cm^{-1}) were discernible. The Raman spectra, as illustrated in Figure S9, indicated the relatively high intensity of the two principal bands (I_D/I_G) in Pt@Co_L SAs.[28] This suggests the presence of a greater number of internal topological defects within the carbon matrix, which is conducive to enhancing the electrical conductivity of the material. The dispersed forms of Pt and Co in the NC substrate were further characterized by using aberration-corrected high-angle annular dark-field scanning transmission electron microscopy (HAADF-STEM). As exhibited in Figure 3c, distinct bright spots can be observed on the Pt@Co_L SAs. The lattice stripe with a spacing of 0.23 nm corresponded to the (111) plane of the Pt particles, indicating that Co mainly dispersed around the Pt particles in the form of single atoms. In contrast, the lattice spacing of 0.207 nm, which corresponds to the (111) plane of the Co particles, was observed in the Pt@Co NPs. The dispersed states of Pt and Co were clearly identifiable (Figure 3d).

To further verify the precise synthesis of each sample, we utilized extended X-ray absorption fine structure (EXAFS) to confirm the local atomic structures of Pt and Co. Figure 3e depicts the EXAFS spectra of the Co K edge. Unlike the presence of Co−N and Co−Co coordination paths in the Pt@Co NPs, only Co−N coordination was present in the Pt@Co_L SAs, confirming the presence of isolated Co sites. The Pt L_3 edge EXAFS spectra in Figure 3f validated the formation of Pt NPs in both Pt@Co_L SAs and Pt@Co NPs, which is in good agreement with the aforementioned results.

Electrocatalytic ORR Performance

The performance for the ORR was evaluated by using both rotating disk electrode (RDE) and rotating ring disk electrode (RRDE) techniques. As show in Figure S10, cyclic voltammetry (CV) analyses were carried out in N_2-saturated 0.1 M $HClO_4$ solution at voltages ranging from 0 to 1.2 V (vs RHE), revealing that the Pt@Co_L SAs exhibited the highest utilization of platinum. Subsequently, linear scanning voltammetry (LSV) measurements in Figure 4a showed that the Pt@Co_L SAs sample exhibits excellent ORR performance ($E_{1/2}$ = 0.92 V, E_{onset} = 1.04 V), significantly outperforming Pt@Co NPs and Pt@ZIF. Impressively, the Pt@Co_L SAs with a lower content of Co single atoms displayed superior performance compared to the Pt@Co_H SAs and also showed significantly improvement over Pt/C ($E_{1/2}$ = 0.86 V, E_{onset} = 0.94 V). It can be inferred that the valence modulation and synergetic electronic interaction contributed to this high ORR catalytic activity. In addition, as shown in Figure 4b, Pt@Co_L SAs achieved optimal mass activity (MA) and specific activity (SA) at both typical potentials (0.85 and 0.9 V), particularly reaching 3.2 A·mg_{Pt}^{-1} and 5.44 mA·cm^{-2} at 0.9 V, representing a 20-fold and 23-fold increase over Pt/C, respectively. To further investigate the reaction mechanisms of Pt@Co_L SAs, LSV tests were conducted at different rotational speeds from 600 to 2500 r·min^{-1}. As the rotational speed increased, the catalyst's onset potential remained constant while the current density gradually increased (Figures S11−S14). The Koutecky−Levich (K-L) plots of Pt@Co_L SAs showed a desirable linear relationship at various potentials, and the slopes of the

https://doi.org/10.1021/prechem.4c00073
Precis. Chem. 2025, 3, 279−288

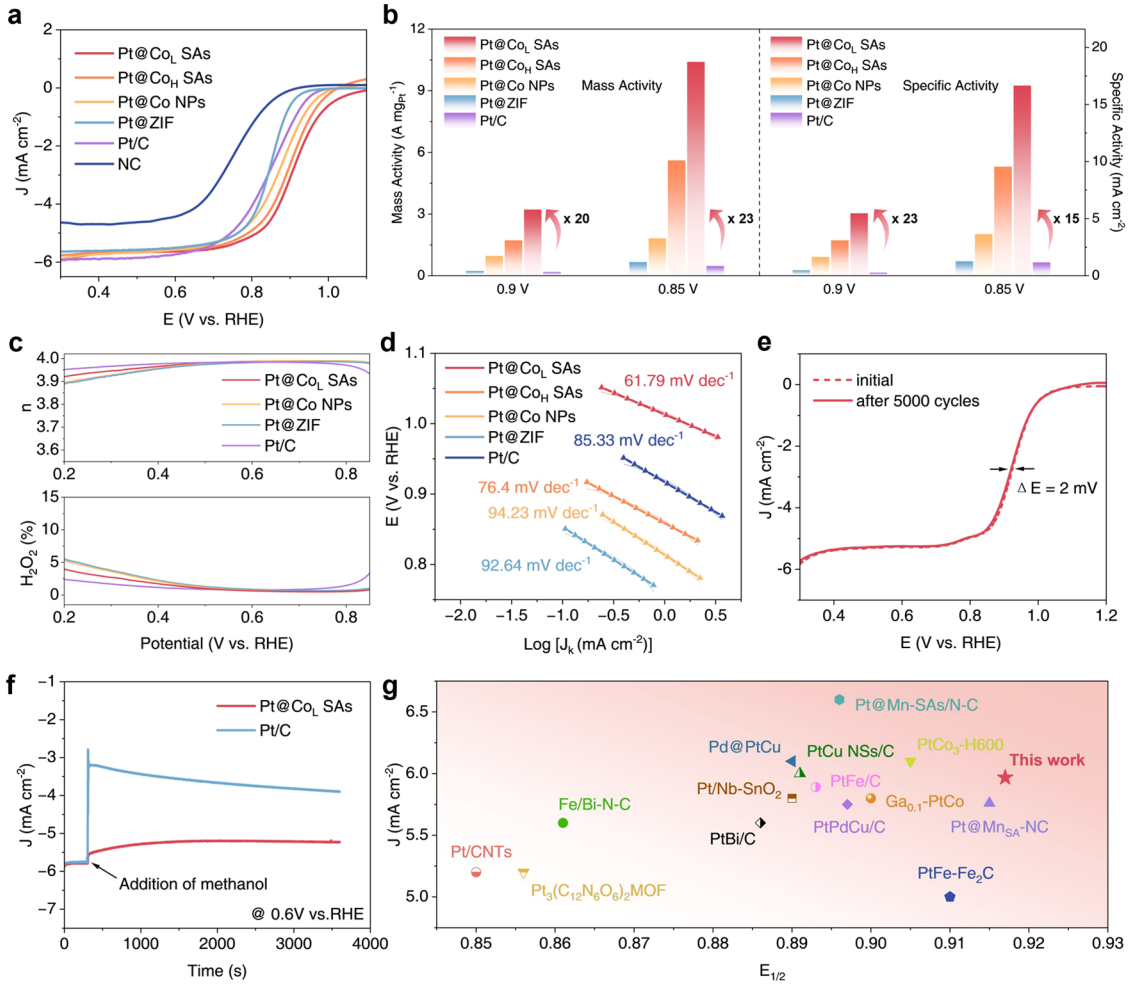

Figure 4. ORR performances in O_2-saturated 0.1 M $HClO_4$. (a) Linear sweep voltammograms (LSVs) for Pt@Co$_L$ SAs, Pt@Co$_H$ SAs, Pt@Co NPs, Pt@ZIF, Pt/C, and NC at 1600 rpm. (b) Mass activity and specific activity comparison of Pt@Co$_L$ SAs, Pt@Co$_H$ SAs, Pt@Co NPs, Pt@ZIF, and Pt/C at potentials of 0.85 and 0.9 V vs RHE. (c) H_2O_2 yield and electron transfer number (n) of Pt@Co$_L$ SAs, Pt@Co NPs, Pt@ZIF, and Pt/C. (d) Corresponding Tafel plots obtained from the RDE polarization curves. (e) ORR polarization LSV curves of Pt@Co$_L$ SAs before and after 5000 cycles. (f) Chronoamperometric responses of Pt@Co$_L$ SAs and Pt/C by adding 0.3 M CH_3OH (at ~300 s) at 0.6 V versus RHE. (g) ORR performance comparison of Pt@Co$_L$ SAs with other reported catalysts.

K-L plots indicate that the catalysts had a typical 4e$^-$ ORR transfer pathway. It was further confirmed by the RRDE testing in Figure 4c, where the electron transfer number (n) of the Pt@Co$_L$ SAs approached the theoretical value of 4 within a potential range of 0.2−0.8 V, and the H_2O_2 yield was less than 5%, indicating the four-electron mechanism akin to commercial Pt/C as confirmed by K-L.

The fast reaction kinetics and excellent activity of Pt@Co$_L$ SAs can be further observed from the smaller Tafel slopes. As shown in Figure 4d, the Tafel slope of Pt@Co$_L$ SAs measured 61.79 mV·dec^{-1}, which was lower than those of Pt@Co$_H$ SAs (76.4 mV·dec^{-1}), Pt@Co NPs (94.23 mV·dec^{-1}), Pt@ZIF (92.64 mV·dec^{-1}), and Pt/C (85.33 mV·dec^{-1}), indicating the fastest reaction kinetics among the compared catalysts. To explore the intrinsic activity of the catalysts, the double-layer capacitance (C_{dl}) was measured. Figure S15 shows the CV curves for different catalysts at scanning rates from 10 to 60 mV·s^{-1}. The C_{dl} value of Pt@Co$_L$ SAs was 27.2 mF·cm^{-2}, which was higher than those of Pt@Co$_H$ SAs (21.4 mF·cm^{-2}), Pt@Co NPs (11.3 mF·cm^{-2}), and Pt@ZIF (9.5 mF·cm^{-2}). This indicated that Pt@Co$_L$ SAs exposed more available catalytically active sites, which was favorable for improving the ORR activity (Figure S16). These results underscore the synergistic effect between Pt and single-atom Co sites as the key to achieving excellent ORR performance. In addition, the stability is another critical indicator for electrochemical evaluations. As shown in Figure 4e, after 5000 cycles in O_2-saturated 0.1 M $HClO_4$ solution, the $E_{1/2}$ of Pt@Co$_L$ SAs decreased by merely 2 mV compared to its initial value, demonstrating superior stability compared to Pt/C (Figure S17). Additionally, the morphology of Pt@Co$_L$ SAs was basically stable after CV acceleration, with only a slight increase in particle size from the original 1.43 to 1.61 nm (Figure S18). More importantly, when considering the application of catalysts in methanol fuel cells, the resistance to methanol poisoning is also particularly important. As depicted in Figure 4f, Pt@Co$_L$ SAs exhibited excellent tolerance to methanol poisoning, whereas Pt/C experienced significant performance degradation in the presence of methanol. Figure 4g and Table S2 highlight that the half-wave potential of Pt@Co$_L$ SAs ranks among the top compared to many other reported acidic ORR catalysts.

https://doi.org/10.1021/prechem.4c00073
Precis. Chem. 2025, 3, 279−288

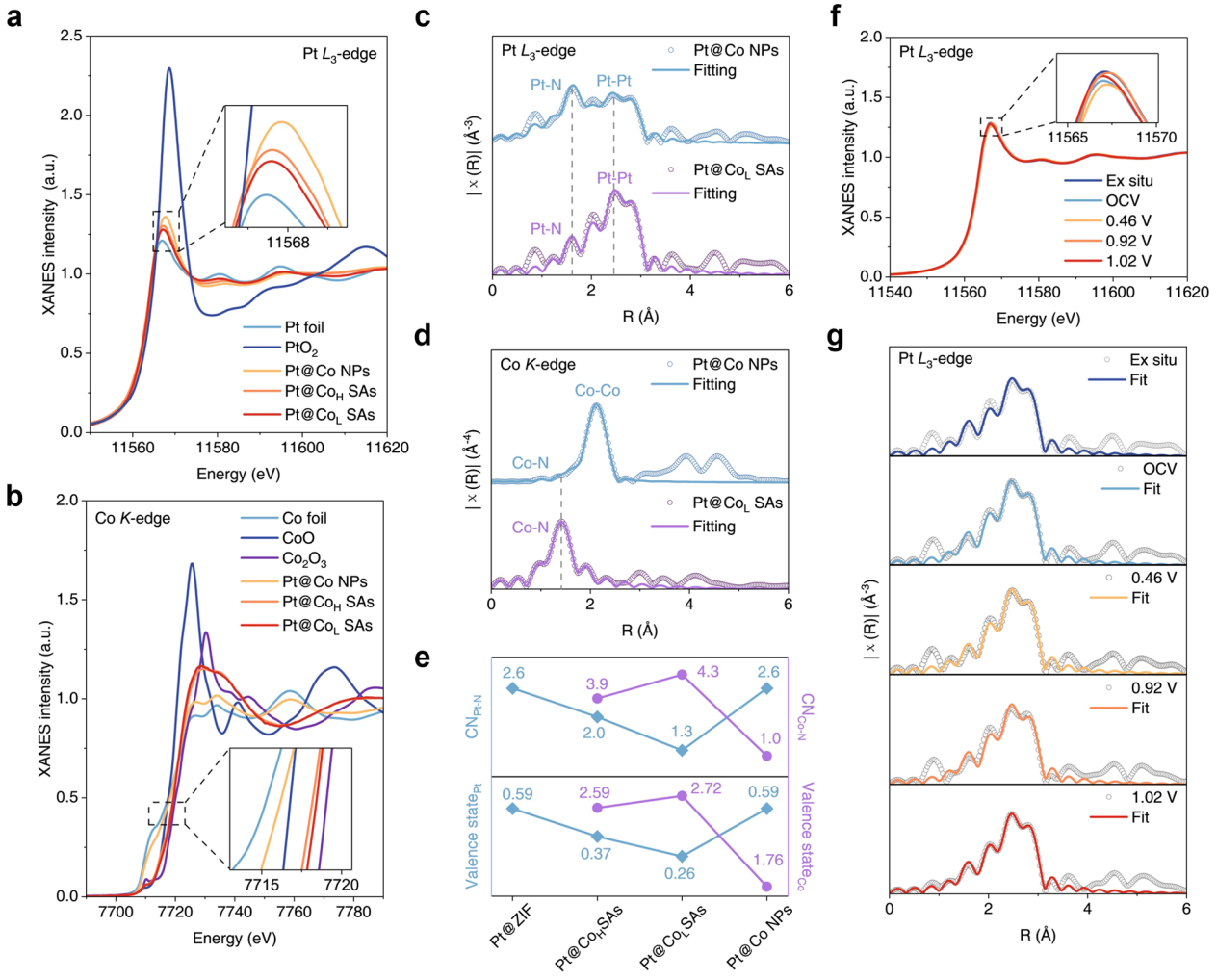

Figure 5. Valence and structure changes at different voltages during electrocatalytic ORR. (a) XANES spectra of Pt L_3 edge of Pt@Co_L SAs, Pt@Co_H SAs, Pt@Co NPs and the reference samples. (b) XANES spectra of Co K edge of Pt@Co_L SAs, Pt@Co_H SAs, Pt@Co NPs, and the reference samples. (c) FT-EXAFS spectra and fitting of the Pt L_3 edge for Pt@Co_L SAs and Pt@Co NPs. (d) FT-EXAFS spectra and fitting of the Co K edge for Pt@Co_L SAs and Pt@Co NPs. (e) Relationship between coordination numbers of Pt−N and Co−N (top). Relationship between the valence states of Pt and Co (bottom). (f) In situ XANES spectra of the Pt L_3 edge, where the inset shows the corresponding local magnifications of the white line peaks. (g) FT-EXAFS spectra at different voltages of the Pt L_3 edge for Pt@Co_L SAs.

Synchrotron X-ray Spectroscopy Characterization

To further investigate the valence and coordination environments of Pt and Co elements in Pt@Co_L SAs, we conducted X-ray absorption near-edge structure (XANES) and EXAFS spectroscopic analyses. The XANES spectra at the Pt L_3 edge in Figure 5a revealed a reduction in the intensity of the white line peak, indicating a decrease in the oxidation state.[29] The white line peak intensities of samples Pt@ZIF, Pt@Co NPs, Pt@Co_H SAs, and Pt@Co_L SAs decreased sequentially, and all remained higher than that of the Pt foil sample, as supported by XPS results (Figure S19). Correspondingly, the absorption edge at the Co K edge shifted rightward,[30] indicating an elevated oxidation state from left to right across Pt@Co NPs, Pt@Co_H SAs, and Pt@Co_L SAs. Meanwhile, comparison with the standard samples found that the positions of the absorption edges for Pt@Co_H SAs and Pt@Co_L SAs were situated between CoO and Co_2O_3, indicating their valence states were located between 0 to +2 and +2 to +3 valence, respectively (Figure 5b). We further analyzed the local atomic structure using EXAFS. (Figures S20−S25). The EXAFS spectra of the Pt L_3 edge illustrated that Pt@Co_L SAs and Pt@Co NPs exhibited a Pt−N coordination peak at about 1.7 Å and a Pt−Pt coordination peak at about 2.5 Å, consistent with the presence of Pt in nanoparticle form (Figure 5c and Table S3). Similar Pt−Pt conformations were observed for Pt@Co_H SAs and Pt@ZIF (Figures S21 and S22). As shown in the EXAFS spectra of the Co K edge in Figure 5d and Table S4, the Pt@Co_L SAs displayed a Co−N peak at approximately 1.4 Å and lacked a distinct Co−Co peak within the 2−3 Å range, which is consistent with the typical features of Co SAs.[31] The peaks with similar features were also found in Pt@Co_H SAs (Figure S24). In contrast, Pt@Co NPs showed a distinct Co−Co peak at 2−3 Å, indicating that Co was present in the form of nanoparticles.[32]

Interestingly, there exists a clear negative correlation between the valence states and coordination numbers of Pt and Co (Figure 5e and Figure S26). The valence states of Co SAs in Pt@Co_L SAs were higher than those of Co NPs in Pt@Co NPs. However, the high valence state of Co resulted in a lower valence state of Pt, which is a direct reflection of the modulation of the electronic structure of Pt by Co. This modulation occurs through metal−support interactions, which

https://doi.org/10.1021/prechem.4c00073
Precis. Chem. 2025, 3, 279−288

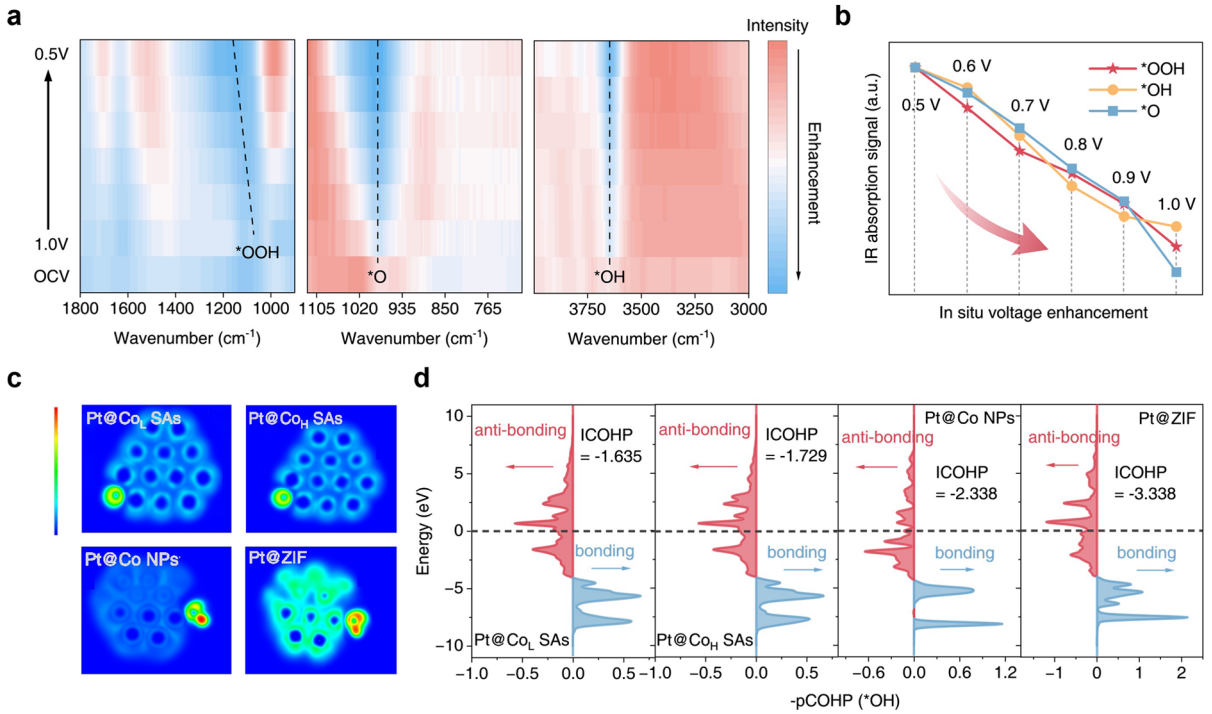

Figure 6. Monitoring of reaction intermediates. (a) *In situ* SR-IR measurements under various potentials for Pt@Co$_L$ SAs during the ORR process. (b) Infrared transmittance signals versus potentials of *O, *OH, and *OOH intermediates. (c) ELF projection plots of Pt@Co$_L$ SAs, Pt@Co$_H$ SAs, Pt@Co NPs, and Pt@ZIF. (d) pCOHP of Pt@Co$_L$ SAs, Pt@Co$_H$ SAs, Pt@Co NPs, and Pt@ZIF. Blue indicates bonding contributions, while red indicates antibonding contributions.

caused a change in the coordination number. Meanwhile, the valence states of Pt and Co show a positive correlation with the coordination number of Pt/Co−N. In order to reveal the nature of the excellent ORR activity and valence state changes in Pt@Co$_L$ SAs, we performed *in situ* XANES and EXAFS spectroscopic measurements to probe their electronic and atomic structure changes. As shown in the Pt L_3 edge XANES spectra and the corresponding local magnification in Figure 5f, the valence state of Pt initially increases and, subsequently, decreases with increasing potential. At 0.46 V vs RHE, the ORR proceeded most vigorously, coinciding with the lowest valence state of Pt.[33−35] Meanwhile, the EXAFS spectra of the Pt L_3 edge at different reaction potentials revealed no obvious changes in the coordination peaks, indicating excellent structural stability of Pt@Co$_L$ SAs (Figure 5g, Figure S27, and Table S5).

In Situ SR-IR Measurements and DFT Calculation

Furthermore, we conducted *in situ* SR-IR tests on Pt@Co$_L$ SAs to investigate the three key intermediates in the ORR process. As shown in Figure 6a, the SR-IR spectra of Pt@Co$_L$ SAs exhibited three distinct infrared peaks located at 1174, 984, and 3648 cm^{-1}, respectively.[36,37] The intensity of these peaks increased as the applied cathodic potential became more negative, indicating the respective intermediates increased with the enhancement of the ORR process (Figure 6b).[38−40] These characteristic peaks correspond to the stretching vibrations of the *OOH, *O, and *OH intermediates, confirming that a 4e$^-$ ORR process occurs at the Pt sites, which is consistent with the suppression of H_2O_2 byproduct (less than 5%) and high electron transfer number. Similar intermediate evolution with potential changes was also observed in both Pt@Co$_L$ SAs and Pt@Co NPs (Figures S28 and S29).

According to theoretical calculations, the desorption of *OH is the main factor affecting the ORR activity. Therefore, we conducted electron localization function (ELF) on the samples and found that Pt@Co$_L$ SAs exhibited the lowest charge densities between *OH and Pt,[41] indicating a weak interaction between them, which was beneficial for the release of *OH and promoted the conversion process of *OH to H_2O (Figure 6c). To further investigate the interaction between Pt and *OH, we conducted a projected crystal orbital Hamilton population (pCOHP) analysis.[42,43] The bond strength can be quantitatively probed by calculating the integral value of the pCOHP part below the Fermi energy level (ICOHP). Figure 6d shows that the ICOHP values of the *OH−Pt bond for Pt@Co$_L$ SAs, Pt@Co$_H$ SAs, Pt@Co NPs, and Pt@ZIF are −1.635, −1.729, −2.338, and −3.338 eV, respectively. This indicated that the *OH−Pt bond adsorbed on Pt@Co$_L$ SAs has the most antibonding state filling, resulting in the weakest adsorption for the *OH intermediate.[44] In summary, Co SAs displayed the best effect in regulating the *OH adsorption energy, reducing the charge accumulation on Pt. The synergistic electronic interaction between Co SAs and Pt catalytic sites is expected to weaken the adsorption of the key intermediate *OH and lower the final reaction energy barrier.

CONCLUSION

In summary, guided by theoretical calculations, we constructed a series of Pt-based catalysts doped with different dispersed states of Co through electronic regulation and intermediate weakening. The catalyst reached a mass activity of 3.2 A·mg$_{Pt}^{-1}$ at a potential of 0.9 V in an acid electrolyte, which is 20× higher than that of Pt/C. The combination of *in situ* XAFS and SR-IR measurements provides in-depth insights into the synergistically promoted mechanism contributing to high-

https://doi.org/10.1021/prechem.4c00073
Precis. Chem. 2025, 3, 279−288

efficiency ORR. The experimental results indicated that Co has a direct regulating effect on the electronic structure of Pt due to the metal host−guest interaction. The interaction between the metal and the support leads to changes in coordination number, resulting in an increase in the valence state of single-atom Co and subsequently regulating the reduction of the Pt valence state. Meanwhile, by weakening the adsorption of the key *OH intermediate product, faster $4e^-$ conversion of intermediate products can be achieved at the Pt sites. This work provides further guidance for regulating the electronic structure of active metals through the precise regulation of Pt by Co in different dispersed states combined with various *in situ* spectroscopic techniques. These findings offer new possibilities for the rational design of advanced ORR electrocatalysts and integrated catalysis of multiple active species.

■ ASSOCIATED CONTENT

Supporting Information

The Supporting Information is available free of charge at https://pubs.acs.org/doi/10.1021/prechem.4c00073.

Details on the materials used, experimental procedures, XRD patterns, TEM, HAADF-STEM images, XPS spectra, $k^2\chi(k)$ and $k^3\chi(k)$ oscillations, cluster models used for calculating Gibbs free energy, LSV and CV curves, and structural parameters derived from EXAFS curve fittings results (PDF)

■ AUTHOR INFORMATION

Corresponding Authors

Dong Liu − *Key Laboratory of Precision and Intelligent Chemistry, School of Nuclear Science and Technology, Hefei National Research Center for Physical Sciences at the Microscale, National Synchrotron Radiation Laboratory, University of Science and Technology of China, Hefei, Anhui 230052, P. R. China*; Email: liudong24@ustc.edu.cn

Tao Ding − *Key Laboratory of Precision and Intelligent Chemistry, School of Nuclear Science and Technology, Hefei National Research Center for Physical Sciences at the Microscale, National Synchrotron Radiation Laboratory, University of Science and Technology of China, Hefei, Anhui 230052, P. R. China*; orcid.org/0000-0001-9143-0679; Email: dingtao@ustc.edu.cn

Tao Yao − *Key Laboratory of Precision and Intelligent Chemistry, School of Nuclear Science and Technology, Hefei National Research Center for Physical Sciences at the Microscale, National Synchrotron Radiation Laboratory, University of Science and Technology of China, Hefei, Anhui 230052, P. R. China*; orcid.org/0000-0001-8699-8294; Email: yaot@ustc.edu.cn

Authors

Yudan Chen − *Key Laboratory of Precision and Intelligent Chemistry, School of Nuclear Science and Technology, Hefei National Research Center for Physical Sciences at the Microscale, National Synchrotron Radiation Laboratory, University of Science and Technology of China, Hefei, Anhui 230052, P. R. China*

Yuanhua Sun − *Key Laboratory of Precision and Intelligent Chemistry, School of Nuclear Science and Technology, Hefei National Research Center for Physical Sciences at the Microscale, National Synchrotron Radiation Laboratory, University of Science and Technology of China, Hefei, Anhui 230052, P. R. China*

Sicheng Li − *Key Laboratory of Precision and Intelligent Chemistry, School of Nuclear Science and Technology, Hefei National Research Center for Physical Sciences at the Microscale, National Synchrotron Radiation Laboratory, University of Science and Technology of China, Hefei, Anhui 230052, P. R. China*

Xiaokang Liu − *Key Laboratory of Precision and Intelligent Chemistry, School of Nuclear Science and Technology, Hefei National Research Center for Physical Sciences at the Microscale, National Synchrotron Radiation Laboratory, University of Science and Technology of China, Hefei, Anhui 230052, P. R. China*

Wei Zhang − *Key Laboratory of Precision and Intelligent Chemistry, School of Nuclear Science and Technology, Hefei National Research Center for Physical Sciences at the Microscale, National Synchrotron Radiation Laboratory, University of Science and Technology of China, Hefei, Anhui 230052, P. R. China*

Qiquan Luo − *Institutes of Physical Science and Information Technology, Anhui University, Hefei, Anhui 230093, P. R. China*; orcid.org/0000-0003-1450-2856

Complete contact information is available at: https://pubs.acs.org/10.1021/prechem.4c00073

Author Contributions

[▽]Y.C., Y.S., and S.L. contributed equally. T.Y., T.D., and D.L. conceived the project and planned the synthesis. Y.C. conducted the material synthesis, physical characterization, and electrochemical tests and analyzed the results. Y.C., D.L., T.D., and T.Y. cowrote the manuscript. Y.C., and S.L. performed the XAFS characterization and analyzed the data. Y.S. and Q.L. conducted the theoretical calculations. All the authors discussed the results and contributed to the manuscript.

Notes

The authors declare no competing financial interest.

■ ACKNOWLEDGMENTS

This work was supported by the National Natural Science Foundation of China (12025505, 22179125, 12205304, and 12405369), the National Key R&D Program of China (2021YFA1600800), the Strategic Priority Research Program of the Chinese Academy of Sciences (XDB0450200), the University of China Innovation Program of Anhui Province (GXXT-2020-053), the Youth Innovation Promotion Association CAS (2022458), USTC research startup funds (KY9990000214), the Fellowship of China Postdoctoral Science Foundation (2021TQ0319, 2024M763159, and BX20240350), Anhui Provincial Natural Science Foundation (2408085QA006), and the Fundamental Research Funds for the Central Universities (WK2060000038, WK2310000125, and WK2310000113). We would like to thank NSRL, BSRF, and SSRF for the synchrotron beam time. We would like to thank the supercomputing system in the Supercomputing Center of University of Science and Technology of China for the calculations. We are grateful for the technical support from Experimental Center of Engineering and Materials Science, USTC. We would thank XFNANO. This work was partially carried out at the Instruments Center for Physical Science, University of Science and Technology of China.

REFERENCES

(1) Du, M.; Li, D.; Liu, S.; Yan, J. Practical Classification of Catalysts for Oxygen Reduction Reactions: Optimization Strategies and Mechanistic Analysis. *Adv. Funct. Mater.* **2023**, *33*, 2301527.

(2) Wang, X. X.; Swihart, M. T.; Wu, G. Achievements, challenges and perspectives on cathode catalysts in proton exchange membrane fuel cells for transportation. *Nat. Catal.* **2019**, *2*, 578−589.

(3) Cheng, H.; Gui, R.; Yu, H.; Wang, C.; Liu, S.; Liu, H.; Zhou, T.; Zhang, N.; Zheng, X.; Chu, W.; et al. Subsize Pt-based intermetallic compound enables long-term cyclic mass activity for fuel-cell oxygen reduction. *Proc. Natl. Acad. Sci. U. S. A.* **2021**, *118*, No. e2104026118.

(4) Zhao, C.-X.; Li, B.-Q.; Liu, J.-N.; Zhang, Q. Intrinsic Electrocatalytic Activity Regulation of M-N-C Single-Atom Catalysts for the Oxygen Reduction Reaction. *Angew. Chem., Int. Ed.* **2021**, *60*, 4448−4463.

(5) Huang, L.; Wei, M.; Qi, R.; Dong, C.-L.; Dang, D.; Yang, C.-C.; Xia, C.; Chen, C.; Zaman, S.; Li, F.-M.; et al. An integrated platinum-nanocarbon electrocatalyst for efficient oxygen reduction. *Nat. Commun.* **2022**, *13*, 6703.

(6) Chen, Y.; Ji, S.; Wang, Y.; Dong, J.; Chen, W.; Li, Z.; Shen, R.; Zheng, L.; Zhuang, Z.; Wang, D.; Li, Y. Isolated Single Iron Atoms Anchored on N-Doped Porous Carbon as an Efficient Electrocatalyst for the Oxygen Reduction Reaction. *Angew. Chem., Int. Ed.* **2017**, *56*, 6937−6941.

(7) Wang, M.; Zhang, Z.; Zhang, S.; Liu, W.; Shang, W.; Su, X.; Liang, Y.; Wang, F.; Ma, X.; Li, Y.; Liu, Y. Non-planar Nest-like $[Fe_2S_2]$ Cluster Sites for Efficient Oxygen Reduction Catalysis. *Angew. Chem., Int. Ed.* **2023**, *62*, No. e202300826.

(8) Mondal, S.; Bagchi, D.; Riyaz, M.; Sarkar, S.; Singh, A. K.; Vinod, C. P.; Peter, S. C. *In Situ* Mechanistic Insights for the Oxygen Reduction Reaction in Chemically Modulated Ordered Intermetallic Catalyst Promoting Complete Electron Transfer. *J. Am. Chem. Soc.* **2022**, *144*, 11859−11869.

(9) Li, M.; Zhao, Z.; Cheng, T.; Fortunelli, A.; Chen, C.-Y.; Yu, R.; Zhang, Q.; Gu, L.; Merinov, B. V.; Lin, Z.; et al. Ultrafine jagged platinum nanowires enable ultrahigh mass activity for the oxygen reduction reaction. *Science* **2016**, *354*, 1414−1419.

(10) Tu, W.; Luo, W.; Chen, C.; Chen, K.; Zhu, E.; Zhao, Z.; Wang, Z.; Hu, T.; Zai, H.; Ke, X.; et al. Tungsten as "Adhesive" in $Pt_2CuW_{0.25}$ Ternary Alloy for Highly Durable Oxygen Reduction Electrocatalysis. *Adv. Funct. Mater.* **2020**, *30*, 1908230.

(11) Li, J.; Chen, M.; Cullen, D. A.; Hwang, S.; Wang, M.; Li, B.; Liu, K.; Karakalos, S.; Lucero, M.; Zhang, H.; et al. Atomically dispersed manganese catalysts for oxygen reduction in proton-exchange membrane fuel cells. *Nat. Catal.* **2018**, *1*, 935−945.

(12) Fu, S.; Zhu, C.; Song, J.; Du, D.; Lin, Y. Metal-Organic Framework-Derived Non-Precious Metal Nanocatalysts for Oxygen Reduction Reaction. *Adv. Energy Mater.* **2017**, *7*, 1700363.

(13) Chung, H. A.-O.; Cullen, D. A.-O.; Higgins, D.; Sneed, B. A.-O.; Holby, E. A.-O.; More, K. L.; Zelenay, P. A.-O. Direct atomic-level insight into the active sites of a high-performance PGM-free ORR catalyst. *Science* **2017**, *357*, 479−484.

(14) Ji, N.; Sheng, H.; Liu, S.; Zhang, Y.; Sun, H.; Wei, L.; Tian, Z.; Jiang, P.; Chen, Q.; Su, J. Boosting oxygen reduction in acidic media through integration of Pt-Co alloy effect and strong interaction with carbon defects. *Nano Res.* **2024**, *17*, 7900−7908.

(15) Zhang, H.; Chen, H.-C.; Feizpoor, S.; Li, L.; Zhang, X.; Xu, X.; Zhuang, Z.; Li, Z.; Hu, W.; Snyders, R.; et al. Tailoring Oxygen Reduction Reaction Kinetics of Fe-N-C Catalyst via Spin Manipulation for Efficient Zinc-Air Batteries. *Adv. Mater.* **2024**, *36*, 2400523.

(16) Han, A.; Sun, W.; Wan, X.; Cai, D.; Wang, X.; Li, F.; Shui, J.; Wang, D. Construction of Co_4 Atomic Clusters to Enable Fe-N_4 Motifs with Highly Active and Durable Oxygen Reduction Performance. *Angew. Chem., Int. Ed.* **2023**, *62*, No. e202303185.

(17) Wang, R.; Zhang, P.; Wang, Y.; Wang, Y.; Zaghib, K.; Zhou, Z. ZIF-derived Co-N-C ORR catalyst with high performance in proton exchange membrane fuel cells. *Prog. Nat. Sci.: Mater. Int.* **2020**, *30*, 855−860.

(18) Yin, P.; Yao, T.; Wu, Y.; Zheng, L.; Lin, Y.; Liu, W.; Ju, H.; Zhu, J.; Hong, X.; Deng, Z.; et al. Single Cobalt Atoms with Precise N-Coordination as Superior Oxygen Reduction Reaction Catalysts. *Angew. Chem., Int. Ed.* **2016**, *55*, 10800−10805.

(19) Xu, H.; Cheng, D.; Cao, D.; Zeng, X. C. RETRACTED ARTICLE: A universal principle for a rational design of single-atom electrocatalysts. *Nat. Catal.* **2018**, *1*, 339−348.

(20) Zhang, J.; Zhang, T.; Ma, J.; Wang, Z.; Liu, J.; Gong, X. ORR and OER of Co-N codoped carbon-based electrocatalysts enhanced by boundary layer oxygen molecules transfer. *Carbon* **2021**, *172*, 556−568.

(21) Wang, T.; Zhang, Y.; Huang, B.; Cai, B.; Rao, R. R.; Giordano, L.; Sun, S.-G.; Shao-Horn, Y. Enhancing oxygen reduction electrocatalysis by tuning interfacial hydrogen bonds. *Nat. Catal.* **2021**, *4*, 753−762.

(22) Guo, W.; Gao, X.; Zhu, M.; Xu, C.; Zhu, X.; Zhao, X.; Sun, R.; Xue, Z.; Song, J.; Tian, L.; et al. A closely packed $Pt_{1.5}Ni_{1-x}$/Ni-N-C hybrid for relay catalysis towards oxygen reduction. *Energy Environ. Sci.* **2023**, *16*, 148−156.

(23) Chen, Z.; Liao, X.; Sun, C.; Zhao, K.; Ye, D.; Li, J.; Wu, G.; Fang, J.; Zhao, H.; Zhang, J. Enhanced performance of atomically dispersed dual-site Fe-Mn electrocatalysts through cascade reaction mechanism. *Appl. Catal., B* **2021**, *288*, 120021.

(24) Liang, L.; Jin, H.; Zhou, H.; Liu, B.; Hu, C.; Chen, D.; Wang, Z.; Hu, Z.; Zhao, Y.; Li, H.-W.; et al. Cobalt single atom site isolated Pt nanoparticles for efficient ORR and HER in acid media. *Nano Energy* **2021**, *88*, 106221.

(25) Rodríguez-Proenza, C. A.; Palomares-Báez, J. P.; Chávez-Rojo, M. A.; García-Ruiz, A. F.; Azanza-Ricardo, C. L.; Santoveña-Uribe, A.; Luna-Bárcenas, G.; Rodríguez-López, J. L.; Esparza, R. Atomic Surface Segregation and Structural Characterization of PdPt Bimetallic Nanoparticles. *Materials* **2018**, *11*, 1882.

(26) Felici, R.; Pedio, M.; Borgatti, F.; Iannotta, S.; Capozi, M.; Ciullo, G.; Stierle, A. X-ray-diffraction characterization of Pt (111) surface nanopatterning induced by C_{60} adsorption. *Nat. Mater.* **2005**, *4*, 688−692.

(27) Wang, P.; Ren, Y.; Wang, R.; Zhang, P.; Ding, M.; Li, C.; Zhao, D.; Qian, Z.; Zhang, Z.; Zhang, L.; Yin, L. Atomically dispersed cobalt catalyst anchored on nitrogen-doped carbon nanosheets for lithium-oxygen batteries. *Nat. Commun.* **2020**, *11*, 1576.

(28) Wu, Q.; Jia, Y.; Liu, Q.; Mao, X.; Guo, Q.; Yan, X.; Zhao, J.; Liu, F.; Du, A.; Yao, X. Ultra-dense carbon defects as highly active sites for oxygen reduction catalysis. *Chem.* **2022**, *8*, 2715−2733.

(29) Wang, C.; Chen, S.; Xie, H.; Wei, S.; Wu, C.; Song, L. Atomic Sn^{4+} Decorated into Vanadium Carbide MXene Interlayers for Superior Lithium Storage. *Adv. Energy Mater.* **2019**, *9*, 1802977.

(30) Jin, Z.; Li, P.; Meng, Y.; Fang, Z.; Xiao, D.; Yu, G. Understanding the inter-site distance effect in single-atom catalysts for oxygen electroreduction. *Nat. Catal.* **2021**, *4*, 615−622.

(31) Zhu, Y.; Wang, J.; Koketsu, T.; Kroschel, M.; Chen, J.-M.; Hsu, S.-Y.; Henkelman, G.; Hu, Z.; Strasser, P.; Ma, J. Iridium single atoms incorporated in Co_3O_4 efficiently catalyze the oxygen evolution in acidic conditions. *Nat. Commun.* **2022**, *13*, 7754.

(32) Cheng, G.; Carter, J. D.; Guo, T. Investigation of Co nanoparticles with EXAFS and XANES. *Chem. Phys. Lett.* **2004**, *400*, 122−127.

(33) Su, H.; Zhou, W.; Zhou, W.; Li, Y.; Zheng, L.; Zhang, H.; Liu, M.; Zhang, X.; Sun, X.; Xu, Y.; et al. *In-situ* spectroscopic observation of dynamic-coupling oxygen on atomically dispersed iridium electrocatalyst for acidic water oxidation. *Nat. Commun.* **2021**, *12*, 6118.

(34) Wang, J.; Hsu, C.-S.; Wu, T.-S.; Chan, T.-S.; Suen, N.-T.; Lee, J.-F.; Chen, H. M. *In situ* X-ray spectroscopies beyond conventional X-ray absorption spectroscopy on deciphering dynamic configuration of electrocatalysts. *Nat. Commun.* **2023**, *14*, 6576.

(35) Zhao, W.; Xu, G.; Dong, W.; Zhang, Y.; Zhao, Z.; Qiu, L.; Dong, J. Progress and Perspective for *In Situ* Studies of Oxygen Reduction Reaction in Proton Exchange Membrane Fuel Cells. *Adv. Sci.* **2023**, *10*, 2300550.

https://doi.org/10.1021/prechem.4c00073
Precis. Chem. 2025, 3, 279−288

(36) Mondal, S.; Bagchi, D.; Riyaz, M.; Sarkar, S.; Singh, A. K.; Vinod, C. P.; Peter, S. C. In Situ Mechanistic Insights for the Oxygen Reduction Reaction in Chemically Modulated Ordered Intermetallic Catalyst Promoting Complete Electron Transfer. *J. Am. Chem. Soc.* **2022**, *144*, 11859−11869.
(37) Hu, H.; Wang, J.; Liao, K.; Chen, Z.; Zhang, S.; Sun, B.; Wang, X.; Ren, X.; Lin, J.; Han, X. Clarifying the Active Structure and Reaction Mechanism of Atomically Dispersed Metal and Nonmetal Sites with Enhanced Activity for Oxygen Reduction Reaction. *Adv. Mater.* **2025**, *37*, 2416126.
(38) Pan, Y.; Ma, X.; Wang, M.; Yang, X.; Liu, S.; Chen, H.-C.; Zhuang, Z.; Zhang, Y.; Cheong, W.-C.; Zhang, C.; et al. Construction of N, P Co-Doped Carbon Frames Anchored with Fe Single Atoms and Fe_2P Nanoparticles as a Robust Coupling Catalyst for Electrocatalytic Oxygen Reduction. *Adv. Mater.* **2022**, *34*, 2203621.
(39) Wang, M.; Zheng, X.; Qin, D.; Li, M.; Sun, K.; Liu, C.; Cheong, W.-C.; Liu, Z.; Chen, Y.; Liu, S.; et al. Atomically Dispersed CoN_3C_1-TeN_1C_3 Diatomic Sites Anchored in N-Doped Carbon as Efficient Bifunctional Catalyst for Synergistic Electrocatalytic Hydrogen Evolution and Oxygen Reduction. *Small* **2022**, *18*, 2201974.
(40) Lin, L.; Ni, Y.; Shang, L.; Sun, H.; Zhang, Q.; Zhang, W.; Yan, Z.; Zhao, Q.; Chen, J. Atomic-Level Modulation-Induced Electron Redistribution in Co Coordination Polymers Elucidates the Oxygen Reduction Mechanism. *ACS Catal.* **2022**, *12*, 7531−7540.
(41) Chen, Y.; Sun, F.; Tang, Q. Computational Insights and Design of Promising Ultrathin PdM Bimetallenes for Oxygen Reduction Electrocatalysis. *Small Methods* **2023**, *7*, 2300276.
(42) Deringer, V. L.; Tchougréeff, A. L.; Dronskowski, R. Crystal Orbital Hamilton Population (COHP) Analysis As Projected from Plane-Wave Basis Sets. *J. Phys. Chem. A* **2011**, *115*, 5461−5466.
(43) Hao, Y.; Wang, L.; Huang, L.-F. Lanthanide-doped MoS_2 with enhanced oxygen reduction activity and biperiodic chemical trends. *Nat. Commun.* **2023**, *14*, 3256.
(44) Liu, Y.; Liu, X.; Lv, Z.; Liu, R.; Li, L.; Wang, J.; Yang, W.; Jiang, X.; Feng, X.; Wang, B. Tuning the Spin State of the Iron Center by Bridge-Bonded Fe-O-Ti Ligands for Enhanced Oxygen Reduction. *Angew. Chem., Int. Ed.* **2022**, *61*, No. e202117617.

https://doi.org/10.1021/prechem.4c00073
Precis. Chem. 2025, 3, 279−288